A seeding system for large-scale Tomographic PIV in aerodynamics

Caridi, Giuseppe; Ragni, D; Sciacchitano, A; Scarano, Fulvio

Publication date
2015

Document Version
Accepted author manuscript

Published in
Proceedings of the 11th international symposium on particle image velocimetry , PIV15

11TH INTERNATIONAL SYMPOSIUM ON PARTICLE IMAGE VELOCIMETRY – PIV15
Santa Barbara, California, September 14-16, 2015

A seeding system for large-scale Tomographic PIV in aerodynamics

Giuseppe Carlo Alp Caridi[1], Daniele Ragni[1], Andrea Sciacchitano[1] and Fulvio Scarano[1]

[1] Department of Aerospace Engineering, TU Delft, The Netherlands
G.Caridi@tudelft.nl

ABSTRACT

Aerodynamic experiments have been conducted at unprecedented large-scale with time-resolved Tomographic Particle Image Velocimetry in a low-speed wind tunnel. The seeding system makes use of helium-filled soap bubbles (HFSB) of 300 μm diameter as flow tracers. HFSBs are characterized by higher scattering efficiency than conventional PIV seeding, which allows the use of state-of-the-art lasers to achieve measurement volumes approaching cubic meters. The performance of the seeding system is inquired looking at the relationship between production rate of HFSB and dynamic spatial range (DSR) of measurement. This relation is derived and compared to the measured results. Experiments are conducted in a large low-speed wind tunnel where a vertical axis wind turbine (VAWT) of 1 m diameter is installed. Time resolved Tomographic PIV measurements are conducted in a measurement volume of 40×20×20 cm^3, allowing to visualize and study the tip vortex motion and evolution in both instantaneous and phase-locked measurements.

1 INTRODUCTION

Tomographic PIV has been used in a wide range of applications since its introduction in 2006 [1]. One of the recognized restrictions of this technique is the extent of the measurement volume, limited to a typical size up to a few hundreds of cubic centimeters [2], especially in airflow experiments where micron-size particle tracers are utilized. As a consequence, Tomo-PIV does not comply yet with the typical requirements for industrial applications, where larger measurement regions are required, especially when the flow topology is dominated by three-dimensional vortical structures. The main factor precluding the upscaling of the technique is the limited laser pulse energy when distributed over a large volume and the in-focus imaging condition imposing a small optical aperture. As a result, the particle peak intensity recorded by the cameras scales inversely to the fourth power of the measurement domain linear size [3]. The use of larger tracer particles has been proposed as a mean to increase the scattered intensity at the expense of the tracing fidelity, which rapidly degrades with the droplet mass and inertia [4]. The neutral buoyancy condition reached with sub-millimeter helium-filled soap bubbles (HFSB) tracers has been recently shown to yield a good tracing fidelity (response time 10-30 μs), suitable for quantitative studies in low-speed aerodynamics [5].

The use of HFSB as flow tracers dates back to the visualization of several aerodynamic flows, including the flow around a parachute [6, 7], the separated flow around an airfoil [8], wing-tip vortices [9] and jet flows [10]. At low concentration, HFSB tracers have been mostly used to visualize individual path-lines within complex flows. However, the low seeding production rate of 10^3-10^4 bubbles per second [11, 12, http://www.sageaction.com/] yields insufficient tracers concentration for PIV image analysis. Moreover, uniform tracer dispersion in the airflow cannot be achieved with the use of a single point source of tracers.

In a previous work from the authors [5], a system based on a single bubble generator with production rate in the order of 50,000 bubbles per second was coupled with an accumulator. A larger amount of tracers were injected in the settling chamber of a small wind tunnel realizing time-resolved tomographic PIV measurements over a domain of approximately 20×20×10 cm^3.

A number of questions remains open, namely the achievable spatial resolution and spatial dynamic range of large scale experiments realized with these tracers. The applicability of these systems in large-scale wind tunnels (test section of 10 m^2 or larger) is also to be assessed before tomographic PIV can become a viable approach to aerodynamic research at industrial scale.

The present study is structured in two parts. The relationship between HFSB production rate and dynamic spatial range (DSR) achievable in a wind tunnel measurements is first discussed, together with a detailed description of the seeding

system based on the previous work from the authors [5], for time-resolved tomographic PIV in large-scale wind tunnels. A discussion about the theoretical and the measured increase of bubble ejection rate with respect to the isolated bubble generator is given, reporting advantages and bottlenecks of the approach. The technique is then applied to study the tip-vortex evolution in the flow developing in the rotor of a vertical axis wind turbine (VAWT) of 1 m diameter and 1 m height. An unprecedented measurement volume for time-resolved Tomo PIV (40×20×20 cm^3) is obtained, allowing to follow the blade passage and the associated tip vortex, along with its formation and spatio-temporal evolution in the inner rotor region.
The measurements are carried out at similar conditions reported in the experiments of Tescione *et al.* [13], where the domain with employment of a scanning system of high resolution stereo PIV in the region of interest with multiple planes and producing a three-dimensional phase-averaged representation of the turbine flow field.

2 SPATIAL RESOLUTION AND DYNAMIC SPATIAL RANGE

In this section, the relationship between the production rate of the HFSB and the *DSR* achievable in tomographic PIV measurements is discussed. Following the approach of Adrian [14], the dynamic spatial range is defined as the ratio between the largest and the smallest resolvable spatial wave length. Later, Westerweel *et al.* [15] specify the spatial dynamic range as the ratio between the length of the field of view L and the particle tracer displacement Δx namely:

$$DSR = \frac{L}{\Delta x} \tag{1}$$

Further studies conducted on the spatial resolution of PIV [16, 17, 18] suggest to use the (linear) size of the interrogation window l_I (or interrogation volume I_V in tomographic PIV) instead of the particle tracer displacement. This is justified by the fact that the measurement spatial resolution is not directly connected with the pulse separation time. Instead, varying the window size has a direct implication on the resolvable scales. As a result, equation 1 can be rewritten as:

$$DSR = \frac{L}{I_V} \tag{2}$$

The above ratio can also be interpreted as the number of independent vectors along a chosen direction within the measurement domain. The minimum size of the interrogation volume in tomographic PIV must comprise 5 to 10 tracers (image number density N_I = 5-10) [2]. As a result, the interrogation volume size depends on the average particle concentration C. For a uniform distribution of tracers, the interrogation volume reads as:

$$I_V = \sqrt[3]{\frac{N_I}{C}} \tag{3}$$

Where N_I represents the particle image number density, defined as the number of particle images per interrogation volume, and C is expressed in number of tracers per unit of volume. Therefore, the dynamic spatial range reads as:

$$DSR = \frac{L}{I_V} = L \left(\frac{C}{N_I}\right)^{\frac{1}{3}} \tag{4}$$

Usually the size of the measurement domain (L) is defined by the geometry of the model and the features of interest in the flow (e.g. the diameter of a cylinder and the length of its wake). The particle image density is chosen in order to maximize the spatial resolution and the mean effective number of particle image pairs for the cross-correlation analysis. As a consequence, the concentration is the parameter most easily varied to achieve the desired *DSR*. When using HFSB tracers, varying the concentration is not easy considering the assumption that the bubbles are used only once after they are released from the emitter. In this respect, the relation between the spatial concentration and the rate of generation $\dot{N}$ can be explicitly expressed. Let us assume that the tracers are travelling within a stream tube of chosen cross section A_{mv} with a velocity u_∞. The rate at which the bubbles cross a plane normal to their direction of convection is given by:

$$\dot{N} = C\, A_{mv}\, u_\infty \tag{5}$$

A simple example is given here to illustrate the requirements in terms of bubble production rate. Let us assume that a stream tube with velocity of 10 m/s of 1 m diameter is to be seeded at a concentration of 5 bubbles/cm^3 (I_V = 1 cm). The generation system needs to supply 50×10^6 bubbles/s, which are approximately 1,000 larger than the production rate of a single generator. The resulting *DSR* for such conditions reaches 100, which well compares to that of many planar PIV experiments reported in the literature [19].
Substituting *C*, obtained from last expression, in equation 4, the *DSR* reads now as:

$$DSR = L\left(\frac{\dot{N}}{N_I A_{mv} u_\infty}\right)^{\frac{1}{3}} \approx \left(\frac{L\,\dot{N}}{N_I\,u_\infty}\right)^{\frac{1}{3}} \tag{6}$$

Where A_{mv} is assumed of order of magnitude L^2. From the last equation, it can be deduced that the *DSR* depends on the characteristic length of the measurement volume, the amount of HFSB entering the measurement volume per unit of time and the free stream velocity.
The bubble rate in the measurement volume, $\dot{N}$, plays a fundamental role to set the required *DSR*. High values of $\dot{N}$ yield a high concentration, which increases the dynamic spatial range. On the other hand, as in every tomographic PIV experiments, the number of *ghost particles* [20] increases rapidly with the density of particle images, which affects the accuracy of tomographic reconstruction and motion analysis, as discussed in the work of Elsinga *et al.* [21]. However, as shown in recent experiment with HFSB [5], the particle image density levels achieved is far below the critical value of 0.05 ppp suggested in the work of Elsinga *et al.* [1].
Instead, the *DSR* is inversely proportional to the free stream velocity u_∞. This additional dependence can be explained once setting a given value for the bubbles production rate.
For a fixed Reynolds number, higher values of *DSR* are achieved increasing the scale of flow and reducing the velocity. In conclusion, it may often be more convenient to scale up the Reynolds number with the geometrical scale instead of increasing the velocity in order to achieve a high *DSR* when using HFSB as flow tracers.

Table 1 - Dynamic spatial range for relevant Tomographic PIV experiments in airflows. (*) Experiment conducted with HFSB. (**) Experiment conducted in a closed volume.

Work in literature	**Measurement domain size *L* [cm]**	**Interrogation box size *I*B [cm]**	***DSR***
Elsinga et al. 2006 [1]	4	2.1	19
Staack et al 2010, [22]	5	0.25	20
Schroder et al 2011 [23]	6.3	0.27	22
Kühn et al. 2011 [24] (*)(**)	75	4.8	15
Fukuchi 2012 [25]	16	0.5	30
Scarano et al. 2015 [5] (*)	20	2	10
Current study (*)	40	2.4	16

A survey of *DSR* retrieved in relevant tomo-PIV experiments is given in Table 1. The dynamic spatial range of tomographic PIV experiments varies between 20 and 30. The recent introduction of HFSB certainly increases the measurement domain size, however with a lower *DSR* mostly ascribed to the poor concentration of the tracers. The latter limitation is partly due to the current unavailability of HFSB generators that can accurately produce neutrally buoyant tracers at rates in the order of 10^7-10^8 bubbles/s. Moreover, the less fundamental, yet very relevant problem of uniformly introducing the tracers upstream of the test section with minimum intrusion to the free-stream flow conditions requires dedicated technical solutions. The remainder of this study describes the concept and the realization of a seeding system that multiplies the instantaneous bubble emission rate from a single generator and that produces a quasi-uniform stream of seeded flow, which can be applied in large scale wind tunnels.

3 SEEDING SYSTEM

The HFSB generator used in the present experiment was provided by LaVision GmbH and it is based on a design made by the German Aerospace Center (DLR). The working principle is described in the work of Bosbach *et al.* [26]. The present bubble generator has the highest production rate, 50000 bubbles/s, among other generators reported in the literature [11, 12, 27 http://www.sageaction.com/], as it can be seen in Table 2. At the present, large-scale tomographic PIV experiments could not be performed with the use of a single bubble generator. When the generator is placed directly in the flow, it is able to generate a seeded stream tube with a cross section of approximately 2.5×2.5 cm^2 with approximately Gaussian distribution for the concentration.

Table 2 - Production rate of different HFSB generator used in air flow measurements

Group	Production Rate [bubbles/s]	Reference
Toyota – Tokyo University	3000	[11]
Sage Action Inc.	300-400	http://www.sageaction.com/
Aachen	500	[27]
DLR	50000	[22]

The procedure adopted to increase the number of HFSB for large-scale tomographic PIV measurements uses a dedicated seeding system, schematically shown in Figure 1. The system is based on a large cylindrical reservoir, approximately 70 liters, where the HFSB are temporarily accumulated before being ejected by the piston motion. An electrical linear actuator controls the movement of the piston. The bubbles are transported into the wind tunnel through a flexible pipeline with a diameter of 3.6 cm and a length of 1.7 m. The latter is connected to an injector that distributes the tracers within a stream-tube.

The aerodynamic rake can be placed in the settling chamber of the wind tunnel as done in the experiments reported in [5], or directly placed in the free stream as done in the current experiments. In the latter case, the expected size of the stream tube coincides with the size of the seeder. The geometry of the probe is represented in Figure 2 and consists of an aerodynamic rake from which the HFSB are homogeneously injected in the stream-tube. The rake consists of twelve airfoils arranged over two staggered rows. Each airfoil has 22 orifices with a diameter of 3 mm along the trailing edge. The overall cross section of the rake is 30×30 cm^2.

The production rate of the bubble generator is indicated with $\dot{N}_0$. In the present case $\dot{N}_0$ = 50,000. The piston moves backward at constant speed, increasing the available volume for a time interval Δt_0 (accumulation time). After that, the piston moves forward rapidly and then forward rapidly (Δt_1 releasing time). The total number of bubbles produced during one period of the piston motion is $\dot{N}_0$ $(\Delta t_0 + \Delta t_1)$. In the ideal case of no extinction, the rate at which the bubbles exit the cylindrical reservoir in Δt_1 is $\dot{N}_1$.

$$\dot{N}_1 = \dot{N}_0 \frac{\Delta t_0 + \Delta t_1}{\Delta t_1} \approx \frac{\Delta t_0}{\Delta t_1} \dot{N}_0 = G\dot{N}_0 \tag{7}$$

The accumulation and releasing times are less than the time life of the bubbles, which is approximately two minutes. In the present case $\Delta t_0 \gg \Delta t_1$. The time ratio $\Delta t_0/\Delta t_1$ represents the gain factor, G, of bubble rate obtained by the seeding system compared to a single bubble generator. Assuming that during the accumulation phase all the bubbles stay in the cylindrical reservoir, whose maximum volume during the accumulation time Δt_0 is V_0, the bubbles concentration within the reservoir is:

$$C_0 = \frac{\dot{N}_0 \Delta t_0}{V_0} \tag{8}$$

At the exit of the seeding system, the bubbles concentration decreases to C due to the air flow passing through the injector when the bubbles are released:

$$C = \frac{\dot{N}_1 \Delta t_1}{V_0 + V_{wt}} = \frac{\dot{N}_0 \Delta t_0}{V_0 + V_{wt}} \tag{9}$$

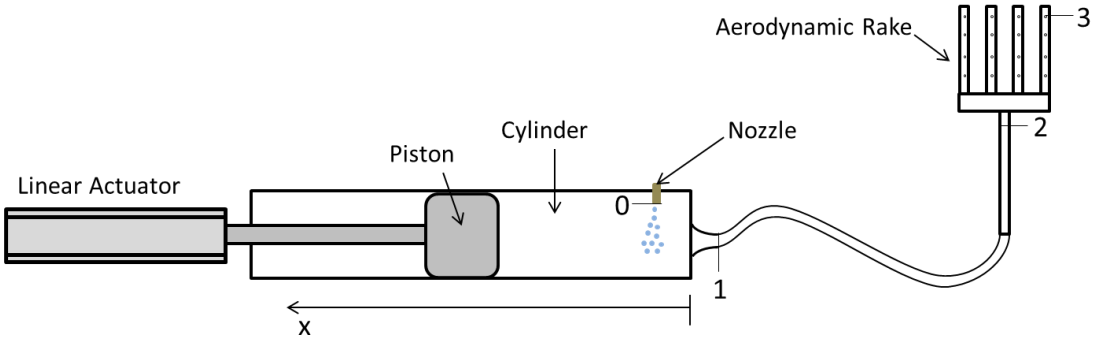

Figure 1 - Schematic of seeding storage and transient injection system.

V_{wt} is the air volume flowing through the diffuser and in which the bubbles are ejected. The term V_{wt} can be expressed as:

$$V_{wt} = A\, v_\infty\, \Delta t_1 \tag{10}$$

Substituting Eq. (10) into Eq. (9), and making use of the definition of the gain factor, the expression of the concentration becomes:

$$C = \frac{\dot{N}_0\, G}{\frac{V_0 + V_{wt}}{\Delta t_1}} = \frac{\dot{N}_0\, G}{\frac{V_0}{\Delta t_1} + A\, u_\infty} = \frac{\dot{N}_0\, G}{\dot{V}_0 + A\, u_\infty} \tag{11}$$

Equation 11 shows the dependence of the concentration from the main working parameters of the seeding system. The choice of the bubble generator determines the bubble rate production, $\dot{N}_0$, and for this reason it plays an important role for the optimization of C. As expected, the concentration of tracers is directly affected by the gain factor, which is easily increased by operating with a longer accumulation time Δt_0. The cross section of the seeded stream-tube A, which is defined by the geometry of the seeding probe, determines the air flow rate in which the bubbles are released and therefore the dilution in the wind tunnel. The size of the injector determines the cross section of the seeded stream tube A. On the other hand, increasing *A* will reduce the concentration of tracers.
Using Eq. 11 with the values in Table 3, corresponding to the experiment described in next section, a theoretical concentration of 3 bubbles/cm^3 was estimated. This concentration allows tomographic PIV measurements on the blade tip-vortex with a diameter of approximately 5 cm, as reported Tescione [13] with planar PIV measurements.

Table 3 - Estimated bubble concentration for the VAWT experiment

$\dot{N}_0$ [b/s]	Δt_0 [s]	Δt_1 [s]	G	V_0 [cm^3]	A [cm^2]	u_∞ [m/s]	C [b/cm^3]
50000	50	1	50	25000	900	8.5	3

Figure 2 - Aerodynamic rake for seeding distribution.

4 EXPERIMENT WITH VERTICAL AXIS WIND TURBINE

The above described system has been applied to perform time resolved tomographic PIV measurements on a scaled model of vertical-axis wind turbine (VAWT). The measurements were conducted in the Open Jet facility (OJF) of TU Delft. The wind tunnel is a closed-circuit with an octagonal cross-section of 2.85×2.85 m^2, driven by a 500 kW electric motor. The model is a two-blade H-shaped rotor VAWT of 1 m diameter (D). The rotor blades consist of NACA0018 aluminum profile of chord c = 0.06 cm. The blades are installed with zero angle of attack. The both blade span H and rotor diameter are 1 m long, yielding an aspect ratio $AR = H/D = 1.0$. Measurements are conducted at free-stream velocity u_∞= 8.5 m/s and rotational speed Ω = 800 rpm, yielding a tip speed ratio $\lambda = 5$. The Reynolds number based on the chord and the tangential velocity of the blades was Re_c = 170,000.

The system of reference and terminology follow the work of Tescione *et al.* [13] on the VAWT and are shown in Figure 3. A Cartesian coordinate system is used with origin at the bottom surface of the blade when it is in the position $\theta = 0°$ (windward position). The free-stream velocity is directed along x from negative to positive values. A positive rotation of the turbine is clockwise if seen from top.
Figure 4 illustrates the arrangement of the seeding system and tomographic system in the wind tunnel. The cylindrical reservoir of the seeding system is visible under the nozzle of the wind tunnel outside the flow field. The seeding probe was mounted at the exit of the wind tunnel at 2.5 m from the VAWT model. A stream tube of tracers is released such that it goes around the bottom tip of the blade when it is at $\theta = 0°$.
The tomographic PIV system consists of a Quantronix Darwin Duo Nd:YLF laser (2×25 mJ at 1 kHz) and three Photron Fast CAM SA1 cameras (CMOS, 1,024×1,024 pixels, 12-bit and pixel pitch 20 μm). The optical magnification is approximately M=0.05 and the extent of the observed region is 38×34×19 cm^3. The lens aperture is set to f/11 in order to ensure images in focus over the entire depth. Under these conditions, images were recorded with a particle density of approximately 0.004 ppp (4,000 particles/Mpixel) and the typical particle peak intensity was 300 counts.

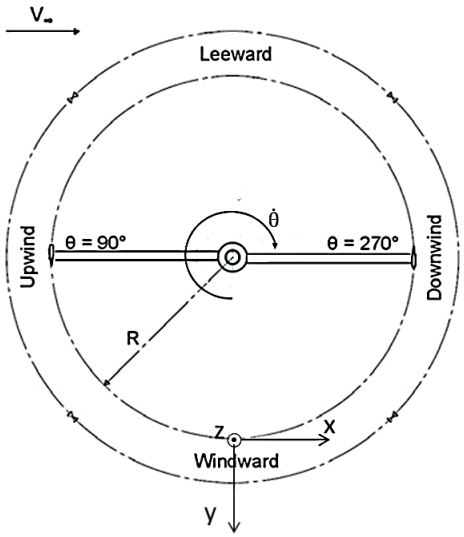

Figure 3 - System of reference and schematic of the blade motion on a vertical axis turbine [13]

Before volume reconstruction, standard image pre-processing for tomo-PIV is conducted, which consists of image background elimination via minimum subtraction and Gaussian filter (3×3 px^2) to regularize the particle image intensity distribution. The domain is discretized into 910×814×456 voxels and reconstructed with a fast MART algorithm. The objects are interrogated with correlation blocks of 80×80×80 voxels (2.4×2.4×2.4 cm^3) and 75 % overlap factor, yielding in a 47×35×24 vectors with a grid spacing of 8 mm. The resulting vector field was post-processed with the universal outlier detection [28].

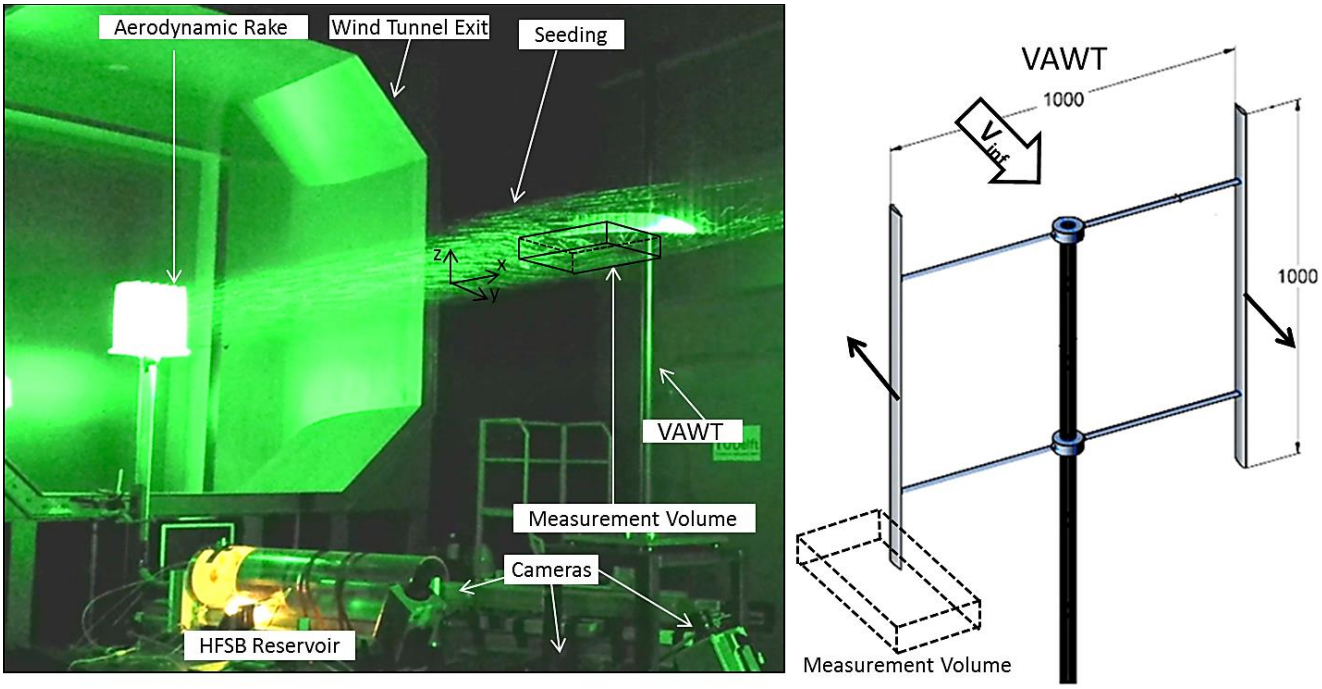

Figure 4 - Arrangement of the experimental set-up, with the HFSB released by the aerodynamic rake installed at the exit of the wind tunnel. Cylindrical reservoir, cameras and indication of the measured volume (left). Sketch of the VAWT with dimensions in millimeters (right).

The LaVision DaVis 8.2.2 software was used for acquisition and processing of the images. Based on particle images count, a concentration of approximately 1 particle/cm^3 is achieved, which correspond to a third of the value estimated in the previous section. The disparity is explained by the bubble losses in the pipeline and in the injector. The recordings are taken at 1 kHz. Figure 5 shows a typical recording.
The quality of tomographic calibration and reconstruction is verified inspecting the reconstructed light intensity distribution along the volume depth (Figure 6). The profile is the average over 100 instantaneous objects and yields a ratio of intensity inside and outside the illuminated region of approximately 7.

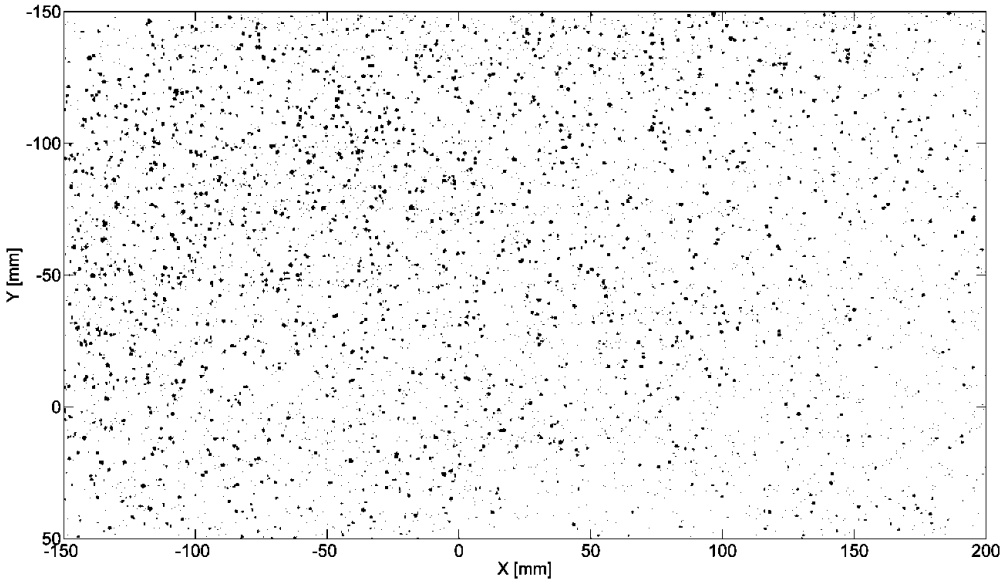

Figure 5 - Raw image from camera 2 (inverted gray levels).

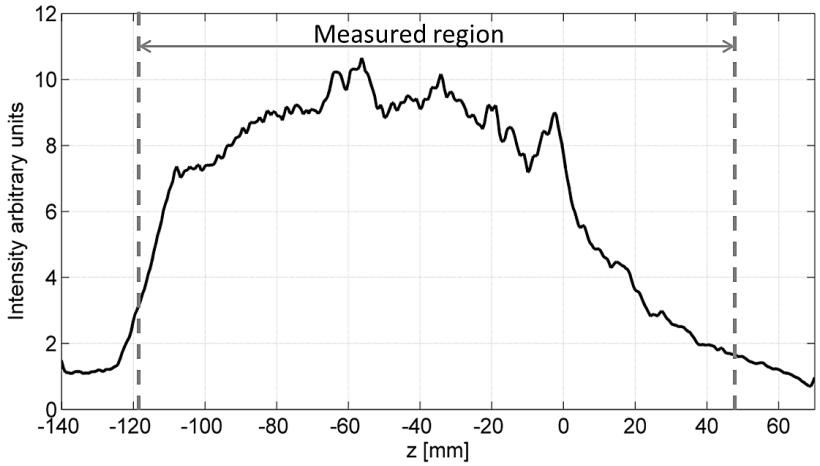

Figure 6 - Spanwise profile of reconstructed light intensity.

4.1 Results

The temporal evolution of the tip vortices generated by the blade motion is illustrated by a sequence of four instantaneous velocity and vorticity fields (Figure 7), at four different angular positions of the blade: $\theta = \{0, 30, 60, 90\}$ degrees, corresponding to time steps of 6 ms. The flow field shows the presence of tip vortices generated by the motion of the retrograding blade from the windward to the upwind position. A portion of the blade is captured inside the measurement volume only for $\theta = 0°$ and $\theta = 30°$ (Figure 7a and 7b). When the blade is at $\theta=0°$, it passes through a zero angle of attack

(no lift) condition. In this respect the only tip vortices that are present in the instantaneous image, indicated as A and B in Figure 7a, have been released by the prior blade and convected downstream.
The blade in Figure 7b has an angle of attack of 30° and is releasing a tip vortex with finite strength, labelled with C. The structures A, B and C are transported downstream by the flow field, where the main component is oriented along the streamwise direction *x*. An outboard component (*z*-direction) is also evident from the side views of Figure 7, where the vortical structures are departing downward from plane *z*=0 towards negative values of *z*.

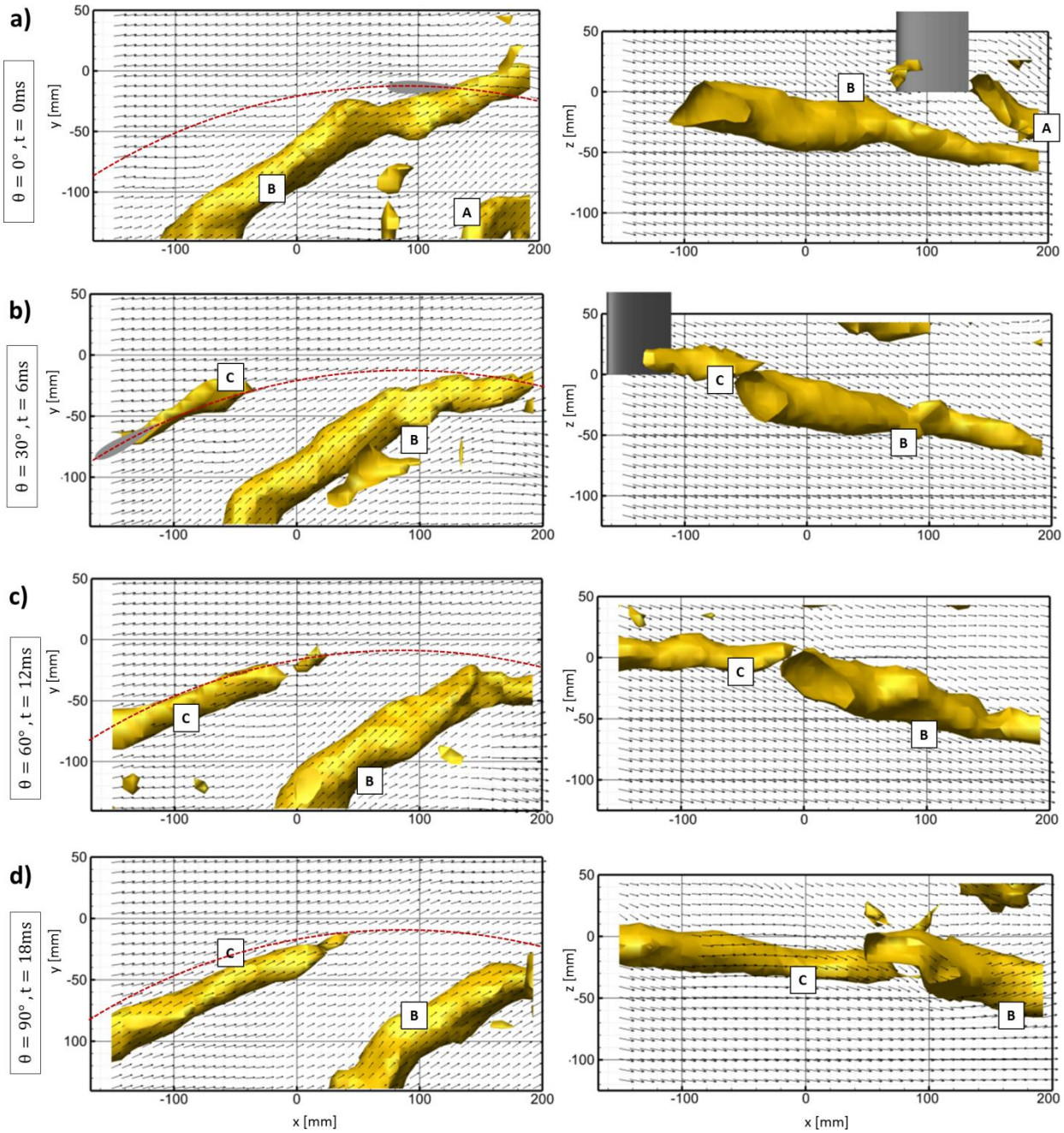

Figure 7 - Top (left) and side view (right) of the instantaneous velocity vector field with vorticity magnitude iso-surface for tip vortices generated by the retrograding blade in a VAWT; Velocity vectors at Z=0 on the left and at Y=-50mm on the right. The blade is at position θ = 0° in (a), θ = 30° in (b), θ = 60° in (c), θ = 90° in (d). Iso-surface corresponds to vorticity magnitude of 240 1/s.

The distance between consecutives tip vortices depends on the tip speed ratio. Along the axis of the tip vortices, a significant increase of the vortex radius is observed. The change of the vortex tube size is related to the variation of the lift generated as the blades rotate through different phase angles θ. The cross section of the tip vortex C released by the blade at θ=0 (Figure 7b) appears narrower than the sections of the same vortex generated with the blade at higher angle of attack (Figure 7c and d). The vortex diameter along the axis of structure B (Figure 7c) was calculated from the iso-surfaces corresponding to vorticity magnitude of 240 1/s with the blade at position $\theta = 60°$. In Figure 8, the phase locked average and ten instantaneous size distributions are plotted along the streamwise direction *x* and show quantitatively a reduction of the vortex size of approximately 30%.

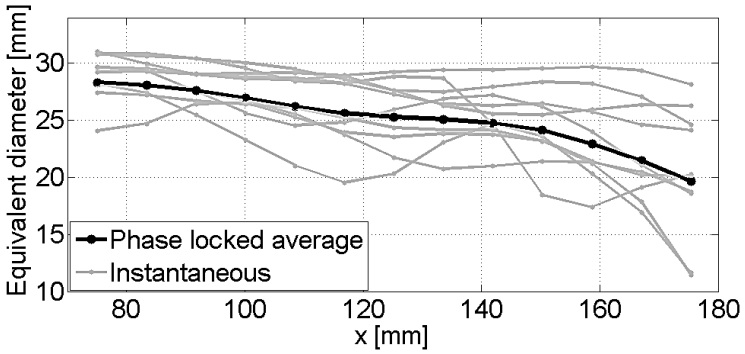

Figure 8 - Size of the tip vortex B (Figure 7) with the blade at position $\theta = 60°$.

Figure 9 shows the evolution of the vortex B, as it was indicated in Figure 7. The local maxima distribution of vorticity of the vortex core is presented along the stream-wise direction *x* at four different angular position θ of the blade, as in Figure 7. Ten instantaneous distributions (grey lines) are presented with the corresponding phase locked average. As has been already mentioned, the tip vortex is transported downstream and the effects of diffusion are negligible. There are no appreciable variations in the peak vorticity magnitude from θ=0° to θ=90° inside the rotor region.

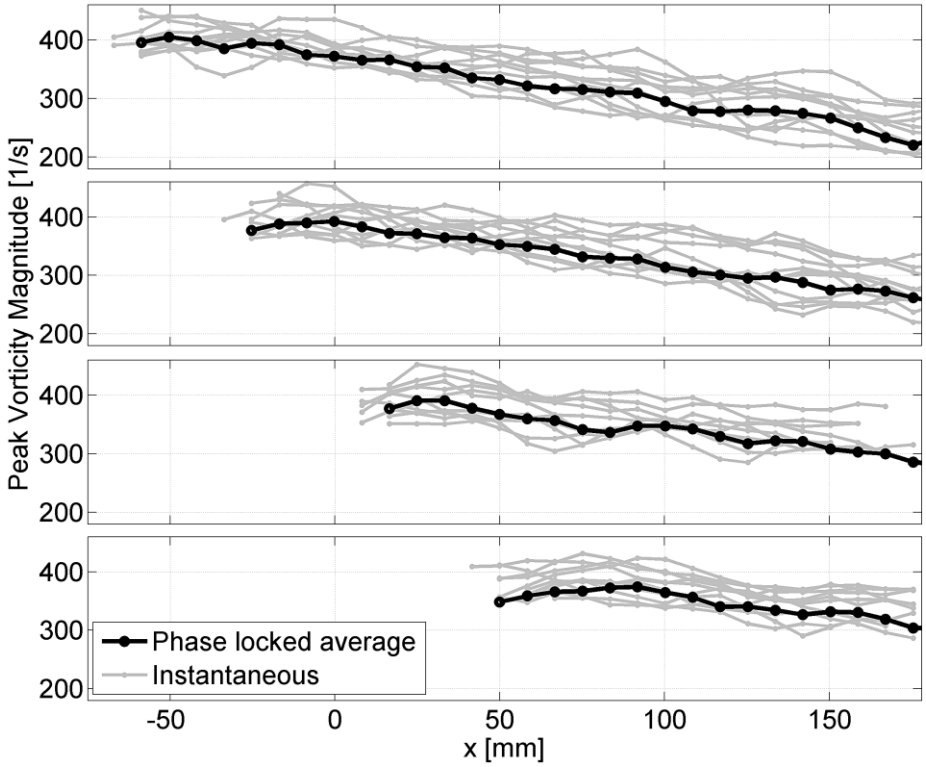

Figure 9 - Peak vorticity magnitude of the tip vortex B (Figure 7) with the blade at position $\theta = 0°$, $\theta = 30°$, $\theta = 60°$, $\theta = 90°$.

5 CONCLUSIONS

In the present study, a relationship between the measurement *DSR* and the production rate of tracer particles has been derived for the case of HFSB seeding systems. The production rate remains the main factor limiting the increase of *DSR* in large-scale tomographic PIV measurements in wind tunnels. A dedicated seeding system was designed to increase the amount of HFSB injected into the flow and it relies upon the accumulation of the HFSB in a reservoir and their release in a time significantly smaller than the accumulation time. The ratio between accumulation and release time determines the gain of bubbles production rate.
The system has been demonstrated in the investigation of the flow dynamics over a vertical axis wind turbine by large-scale time-resolved tomographic PIV. Time-resolved measurements in a volume of 40×20×20 cm^3 were achieved with a seeding concentration of about 1 bubble/cm^3. Data analysis by spatial cross-correlation has yielded the instantaneous large-scale flow structures in the rotor region of the VAWT, where the dynamics of the wing-tip vortex has been documented. The results allow quantitative analysis of the three dimensional vorticity field and the characterisation of the peak vorticity distribution and dynamics.

REFERENCES

[1] Elsinga GE, Scarano F, Wieneke B and Van Oudheusden BW "Tomographic particle image velocimetry" Experiment in Fluids 41 (2006) pp. 933-947

[2] Scarano F "Tomographic PIV: principles and practice" Measurement Science and Technology 24 (2013) pp 012001

[3] Adrian RJ "Particle-imaging techniques for experimental fluid mechanics" Annual review of fluid mechanics" *23*(1) (1991) pp. 261-304

[4] Melling A Tracer particles and seeding for particle image velocimetry, Measurement Science and Technology 8 (1997) pp. 1406

[5] Scarano F, Ghaemi S, Caridi GCA, Bosbach J, Dierksheide U and Sciacchitano A "On the use of helium-filled soap bubbles for large-scale tomographic PIV in wind tunnel experiments" Experiments in Fluids 56(2) (2015) pp. 1-12

[6] Pounder E "Parachute inflation process Wind-Tunnel Study" WADC Technical report 56-391, Equipment Laboratory of Wright-Patterson Air Force Base (1956) pp 17-18, (Ohio,USA)

[7] Klimas P "Helium bubble survey of an opening parachute flowfield" Journal of Aircraft 10 (1973) pp. 5670-5694

[8] Hale RW, Tan P and Ordway DE "Experimental investigation of several neutrally-buoyant bubble generators for aerodynamic flow visualization" Naval Research Review 24 (1971a) pp. 19-24

[9] Hale RW, Tan P, Stowell RC and Ordway DE "Development of an integrated system for flow visualization in air using neutrally-buoyant bubbles" SAI-RR 7107 Sage Action Inc. Ithaca NY USA (1971b)

[10] Ferrell GB, Aoki K and Lilley DG "Flow visualization of lateral jet injection into swirling crossflow" AIAA Paper 85 (1985) pp. 14-17

[11] Okuno Y, Fukuda T, Miwate Y and Kobayashi T "Development of three dimensional air flow measuring method using soap bubbles" JSAE Review 14(4) (1993) pp. 50-55

[12] Müller D, Müller B, and Renz U "Three-dimensional particle-streak tracking (PST) velocity measurements of a heat exchanger inlet flow" Experiments in Fluids 30 (2001) pp. 645-656

[13] Tescione G, Ragni D, He C, Ferreira CS and van Bussel, GJW "Near wake flow analysis of a vertical axis wind turbine by stereoscopic particle image velocimetry" Renewable Energy 70 (2014) pp. 47-61

[14] Adrian RJ "Dynamic ranges of velocity and spatial resolution of particle image velocimetry" Measurement Science and Technology 8(12) (1997) pp. 1393

[15] Westerweel J, Elsinga GE and Adrian, R. J. (2013). Particle image velocimetry for complex and turbulent flows. Annual Review of Fluid Mechanics, *45*, 409-436

[16] Schrijer FFJ and Scarano F "Effect of predictor–corrector filtering on the stability and spatial resolution of iterative PIV interrogation" Experiments in Fluids *45*(5) (2008) pp. 927-941

[17] Astarita T "Adaptive space resolution for PIV" Experiments in fluids *46*(6) (2009) pp. 1115-1123

[18] Kähler CJ, Scharnowski S and Cierpka C "On the resolution limit of digital particle image velocimetry" Experiments in fluids *52*(6) (2012) pp. 1629-1639

[19] Raffel M, Willert CE, Wereley ST and Kompenhans J "Particle Image Velocimetry -A Practical Guide" 2nd edn. Springer (2007)

[20] Maas HG, Gruen A and Papantoniou D "Particle tracking velocimetry in three-dimensional flows" Experiments in Fluids, 15(2) (1993) pp. 133-146

[21] Elsinga GE, Westerweel J, Scarano F and Novara M "On the velocity of ghost particles and the bias errors in Tomographic-PIV" Experiments in Fluids 50(4) (2011) pp. 825-838

[22] Staack K, Geisler R, Schröder A and Michaelis D "3D-3C-coherent structure measurements in a free turbulent jet" 15th Int Symp. on Applications of Laser Techniques to Fluid Mechanics (Lisbon, Portugal) (2010)

[23] Schröder A, Geisler R, Staack K, Elsinga GE, Scarano F, Wieneke B and Westerweel J "Eulerian and Lagrangian views of a turbulent boundary layer flow using time-resolved tomographic PIV" Experiments in Fluids 50 (2011) pp. 1071-1091

[24] Kühn M, Ehrenfried K, Bosbach J and Wagner C "Large-scale tomographic particle image velocimetry using helium-filled soap bubbles" Experiments in Fluids 50 (2011) pp. 929-948

[25] Fukuchi Y "Influence of number of cameras and preprocessing for thick volume Tomographic PIV" 16th Int. Symp. on Applications of Laser Techniques to Fluid Mechanics (Lisbon, Portugal) (2012)

[26] Bosbach J, Kühn M and Wagner C "Large scale particle image velocimetry with helium filled soap bubbles" Experiments in Fluids 46 (2009) pp. 539-547

[27] Müller D, Müller B, and Renz U "Three-dimensional particle-streak tracking (PST) velocity measurements of a heat exchanger inlet flow" Experiments in Fluids 30 (2001) pp. 645-656

[28] Westerweel J and Scarano F "Universal outlier detection for PIV data" Experiments in Fluids 39 (2005) pp. 1096-1100